arXiv:2405.12895v2 [cs.GR] 30 Oct 2024

# Implicit-ARAP: Efficient Handle-Guided Deformation of High-Resolution Meshes and Neural Fields via Local Patch Meshing

DANIELE BAIERI, Sapienza University of Rome, Italy
FILIPPO MAGGIOLI, University of Milano-Bicocca, Italy
ZORAH LÄHNER, University of Bonn, Germany and Lamarr Institute, Germany
SIMONE MELZI, University of Milano-Bicocca, Italy
EMANUELE RODOLÀ, Sapienza University of Rome, Italy

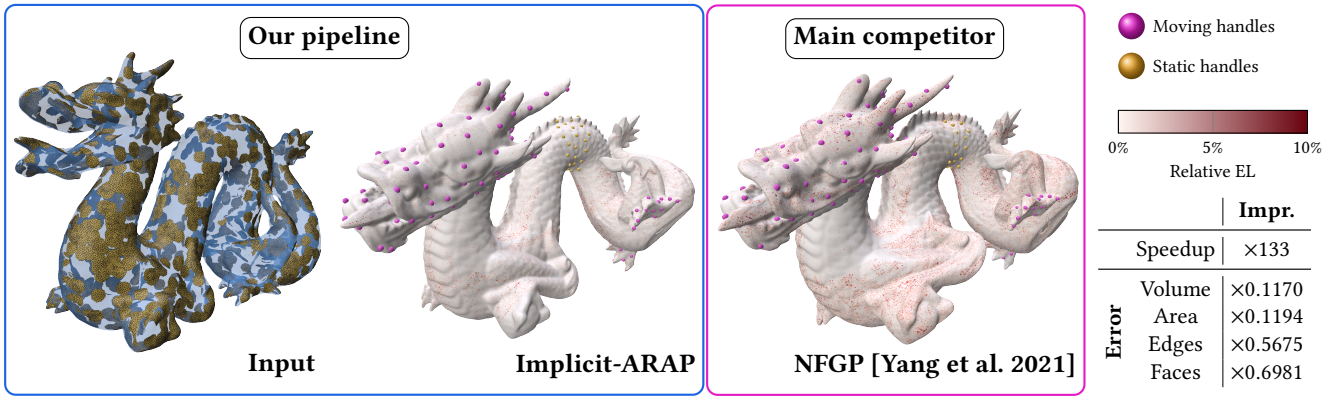



Fig. 1. Given an implicit surface and deformation handles, we employ our local patch mesh representation to compute and optimize the ARAP energy along with a loss to fit the handles. Implicit-ARAP may be used to deform either neural fields directly, or high-resolution meshes after internally converting them to neural fields. Our method introduces significant quality improvements over previous state of the art while only requiring 0.75% of the time. We show the percentual variation in edge lengths as an error map on the deformed surfaces.

In this work, we present the local patch mesh representation for neural signed distance fields. This technique allows to discretize local regions of the level sets of an input SDF by projecting and deforming flat patch meshes onto the level set surface, using exclusively the SDF information and its gradient. Our analysis reveals this method to be more accurate than the standard marching cubes algorithm for approximating the implicit surface. Then, we apply this representation in the setting of handle-guided deformation: we introduce two distinct pipelines, which make use of 3D neural fields to compute As-Rigid-As-Possible deformations of both high-resolution meshes and neural fields under a given set of constraints. We run a comprehensive evaluation of our method and various baselines for neural field and mesh deformation which show both pipelines achieve impressive efficiency and notable improvements in terms of quality of results and robustness. With our novel pipeline, we introduce a scalable approach to solve a well-established geometry processing problem on high-resolution meshes, and pave the way for extending other geometric tasks to the domain of implicit surfaces via local patch meshing.

CCS Concepts: • **Computing methodologies** → **Shape modeling**; *Shape representations*; *Neural networks*; Volumetric models.

Additional Key Words and Phrases: ARAP, Neural Fields, Implicit Representations, Surface Patches

Authors' addresses: Daniele Baieri, baieri@di.uniroma1.it, Sapienza University of Rome, Rome, Italy; Filippo Maggioli, filippo.maggioli@unimib.it, University of Milano-Bicocca, Milan, Italy; Zorah Lähner, laehner@uni-bonn.de, University of Bonn, Bonn, Germany and Lamarr Institute, Germany; Simone Melzi, simone.melzi@unimib.it, University of Milano-Bicocca, Milan, Italy; Emanuele Rodolà, rodola@di.uniroma1.it, Sapienza University of Rome, Rome, Italy.

## 1 INTRODUCTION

Implicit representations, in which the surface of an object is not defined explicitly but implicitly - for example, through the zero level-set of a signed distance function, have been around in computer graphics for a long time but experienced a recent surge of attention due to advances based on NeRF [Mildenhall et al. 2020]. A neural field stored within a neural network has many advantages, like flexibility in topology, no predefined discretization, and the straightforward inclusion in gradient-descent-based methods. These make neural fields optimal choices for reconstruction tasks and, with the wider availability of geometry in this representation, the need for direct analysis and manipulation of implicit representations emerges.

The traditional representation used in geometry processing applications is the polygonal mesh, in which the surface is explicitly modelled by a collection of connected polygons. This representation provides a high level of interpretability and allows for fine-grained manipulation by artists. Additionally, local surface properties can be easily computed because the neighborhood information is explicitly encoded. Due to its wide adaption and easy manipulation, a number of editing methods have been developed for explicit representations: one of them is optimizing the as-rigid-possible (ARAP) energy to deform an object while satisfying user-defined handle constraints and at the same time preserving the surface geometry (in terms of its edges) to a reasonable extent. This yields natural deformations

and has been widely adapted in various applications [Bozic et al. 2020; Huang et al. 2021; Nagata and Imahori 2024].

Evaluating energies such as ARAP directly on implicit surfaces is challenging: properties like edge-length cannot be computed without applying a discretization scheme, and equivalent properties do not necessarily exist for isosurfaces. Alternating between both representations is certainly possible [Mehta et al. 2022], but it is expensive and inherits the sensitivity to discretization choices [Yang et al. 2021]. To counter this, we propose a new patch-based meshing for implicit representations which is 1) efficient to comput even at high resolution, 2) not sensitive to the specific choice of discretization, and 3) can be used on all isosurfaces to cover the complete geometric information of the neural field. Along with local patch meshing, our work proposes multiple other significant contributions:

- Adapting the evaluation of the ARAP energy for handling implicit representations;
- Providing an efficient method for handle-guided deformation of implicit surfaces and neural fields (see Figure 1);
- Introducing a robust and efficient alternative for deforming high-resolution meshes.

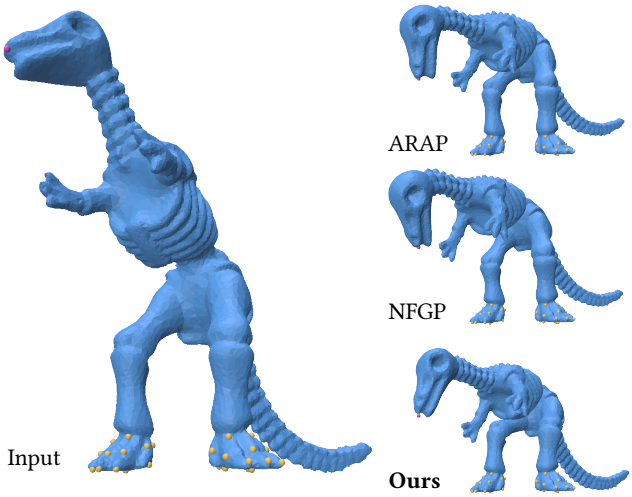



Fig. 2. Replication of one of the experiments from the ARAP paper [Sorkine and Alexa 2007]. Our method directly optimizes for local rigidity energy, but it can converge to visibly different optima than ARAP and NFGP. Interestingly, NFGP's results are closer to ARAP, even with a completely different type of regularization.

## 2 RELATED WORK

*Handle-Based Deformations.* Mesh-based shape editing methods have a long history in geometry processing due to the wide acceptance and explicit representation of meshes [Botsch et al. 2006; Yu et al. 2004]. Among these, methods which use handles to indicate the preferred deformation are intuitive for human users to understand and generate. The as-rigid-as-possible (ARAP) energy [Sorkine and Alexa 2007] has become popular due to its straight-forward interpretation and easy optimization while satisfying handle constraints. However, while not complex, its global nature still prevents processing of high-resolution shapes and is sensitive to the mesh discretization. The second aspect was overcome in SR-ARAP [Levi and Gotsman 2015] with a smoothed and rotation-enhanced ARAP version. While the rigid version is widely used in variety of applications [Bozic et al. 2020; Huang et al. 2021; Nagata and Imahori 2024], there exist similar formulations other energies related to shape deformation, for example conformal [Paries et al. 2007; Vaxman et al. 2015] and elastic deformation energies [Chao et al. 2010]. Instead of using a pre-defined physical energy, it is also possible to learn a set of handles from a collection of shapes [Liu et al. 2021a; Pan et al. 2022]. However, these require a suitable set of training data and are restricted to the space of deformations learned initially.

*Neural Fields Editing.* Energies like ARAP act directly on the deformation of the surface and, thus, are more natural to implement on explicit surface representations like triangle meshes. Editing implicit surfaces is more challenging because of their chaotic behavior: changing a surface locally can have a global effect on the distance field affecting points at high distance. Even locating the surface in space could be non-trivial if one drops some assumptions. The current rise of NeRF-like methods [Mildenhall et al. 2020] has put implicit representations in the spotlight and led several works exploring how to integrate deformations in an implicit framework. Dynamic NeRFs have been realized by adding a time parameter [Pumarola et al. 2020] or by optimizing for a deformation field for the movement [Cai et al. 2022]. A different approach is taken in [Erkoç et al. 2023] and [Berzins et al. 2023] which manipulate the MLP weights of the neural field directly to generate and edit the shapes respectively. While this seems natural, there is no efficient way to formulate explicit energies like ARAP in this way and the optimization is even less efficient than on explicit representations. In [Mehta et al. 2022], shapes can be deformed and interpolated by alternating between evaluation in explicit and implicit representation which can make use of the advantages of both but requires the expensive conversion step in every iteration. Novello *et al.* [Novello et al. 2023] achieves a variety of deformations for neural fields but does not support handle-based constraints. Similarly to our approach, Esturo *et al.* [Esturo et al. 2010] consider all isosurfaces in an implicit function at the same time but optimizes for a volume-preserving deformation which can be represented by a divergence-free deformation field, an approach that does not necessarily depend on implicit fields as shown in [Eisenberger et al. 2019]. Lastly, recent work proposed various methods to perform text-driven editing of implicit geometry encoded in neural [Liu et al. 2021b; Wang et al. 2021] or hybrid [Chen et al. 2023; Fang et al. 2024; Palandra et al. 2024] representations (such as Gaussian splatting).

The method closest to ours is [Yang et al. 2021], which optimizes a deformation loss based on the sampling of an implicit representation and properties that can be derived directly from the neural field. However, this method is very inefficient, taking several hours for a simple example like Figure 2. In contrast, we propose a solution that makes use of the complete information of the neural field, while at

the same time being efficient through the use of small discrete random patches. It is worth noting that there have been other attempt to simplify the local representation of a signed distance field, while at the same time preserving the complexity of the overall structure. On top of the marching cubes algorithm, Theisel [Theisel 2002] proposed to represent the internal structure of the cube using Bézier surfaces instead of simple triangles, producing an analytic explicit equation of the surface. Alternatively, Liu *et al.* [Liu et al. 2023] introduced a method for composing implicit geometric primitives to fit the original surface, providing a simpler and more computationally efficient local representation. However, contrarily to our method, both these approaches fail to provide a local representation that is both explicit and structurally simple.

## 3 METHOD

Our method employs a local patch model (Sec. 3.1) to sample the surface of a neural signed distance field, which is then deformed according to an ARAP-like energy (Sec. 3.2) with an efficient optimization scheme (Sec. 3.3).

### 3.1 Local patch meshing

Given a 3D surface $\mathcal{S}$ represented implicitly by a neural signed distance field $f_\theta\colon \mathbb{R}^3 \to \mathbb{R}$, we require a discrete piece-wise representation in order to compute the ARAP energy induced by a given deformation field $d\colon \mathbb{R}^3 \to \mathbb{R}^3$. We will achieve this by generating local patches for *multiple* isosurfaces of $f_\theta$. The procedure is separated into sampling and projection:

*Sampling.* We start by sampling $k$ points $V = \{v_j\}_{j=1}^k$ from a circle with radius $\rho$ on the 2D plane (including the origin) and computing the planar Delaunay triangulation. We visualize four possible types of discretization in Figure 3. Even though the patches are visibly different both in terms of point distribution and triangle appearance, the specific choice has little influence on our method, as we show in Figure 16.

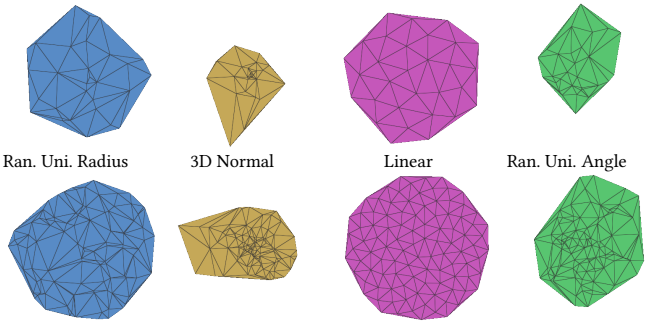



Fig. 3. Different distributions for sampling the 2D circle. From left to right: random uniform radius and angle, 3D normal sampling scaled by maximum norm, linear sampling (deterministic) of radius and angle, normal radius (scaled by maximum value) and uniform angle. Top row: 30 pts per patch. Bottom row: 100 pts per patch.

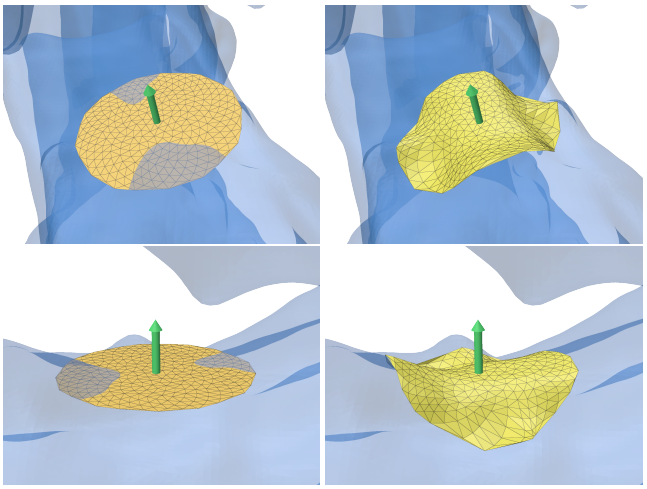


Fig. 4. A linearly sampled patch of 200 points is aligned to the surface normal at a point of the zero level set of the Stanford dragon (left column) via Equation (1). Afterwards, the patch is projected to locally fit the surface (right column) via Equation (2).

*Projection.* Once we obtain the triangular patch $\mathcal{P} = (V, F)$, we will cover each isosurface with a projected version of the patch to represent the geometry. To that end, we uniformly sample $n$ points $O = \{o_i\}_{i=1}^n$ from the zero level set $\mathcal{S}_0$ using the rejection/projection algorithm proposed by Yang *et al.* [Yang et al. 2021]. Additionally, we sample points from other level sets by sampling the 3D interval $[-1; 1]^3$ uniformly at random. We affinely transform each patch so that the origin is centered at $o_i$ and the patch is aligned with the tangent plane at $o_i$, which is inferred from the surface normal extracted from $f_\theta$. The new points of patch $P_i$ are defined as

$$V_i = \left\{o_i + R_i \left(t\left(v_j\right)\right)\right\}_{j=1}^k , \tag{1}$$

where $t$ maps 2D points to 3D as $t\colon (x, y) \mapsto (x, y, 0)$, $o_i$ are the sampled origin points, and $R_i$ are the rotations aligning normal directions at each $o_i$. Afterwards, we map each point of the patches onto the surface by employing the SDF closest surface point formula [Chibane et al. 2020; Yang et al. 2021] which maps any 3D point to its nearest point on a given level set $l$ using

$$p' = p - (f(p) - l)\frac{\nabla f(p)}{\|\nabla f(p)\|} . \tag{2}$$

In practice, when $f$ is a neural SDF, this formula has to be applied recursively to yield accurate results (*i.e.* points whose signed distance is approximately $l$). A visual example for this local patching process is provided in Figure 4. Note that the radius $\rho$ of the tangent disk specifies a measure of locality which is highly dependent on the complexity of the meshed surface $\mathcal{S}$: more complex geometries require a finer-grained sampling – see Figure 5 for an example.

By sampling origin points from all isosurfaces of the signed distance field $f_\theta$, the procedure leads to a complete patching of the neural field. We describe how this structure can be applied to shape deformation in Section 3.3. Moreover, we compare it to the classic SDF meshing algorithm Marching Cubes [Lorensen and Cline

1987a,b] in terms of its properties and benefits in the application to the handle-guided deformation task in Section 5.3.

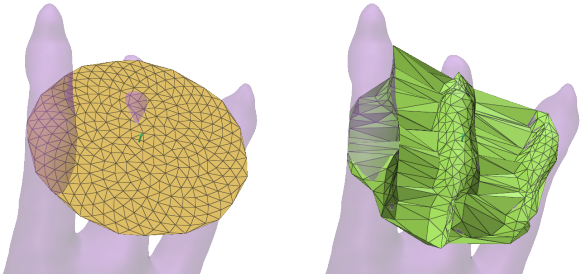


Fig. 5. Our local patch meshing algorithm may incorrectly place triangles outside of the surface when points from the same patch are mapped to different regions of the surface in the deformation step. This may happen when the patch radius $\rho$ is overestimated for some patches.

## 3.2 Deformation model

Since we aim to edit the entire SDF field rather than a set of surface points, we must apply a deformation to the embedding space, which we represent as a continuous function $d\colon \mathbb{R}^3 \to \mathbb{R}^3$. We implement the deformation $d$ via a neural network mapping 3D coordinates to roto-translations, with parameter set $\phi$:

$$T_\phi : x \mapsto \Big(R_\phi(x), t_\phi(x)\Big)\,, \tag{3}$$

$$R_\phi\colon \mathbb{R}^3 \to \mathrm{SO}(3)\,, \tag{4}$$

$$t_\phi : \mathbb{R}^3 \to \mathbb{R}^3\,. \tag{5}$$

Specifically, we model $T_\phi$ with a multilayer perceptron (MLP). The output layer predicts a 6D vector, where the first three components are interpreted as Euler angles and converted to a rotation matrix. In the following, we will refer to the rotation field as $R_\phi$ and to the translation field as $t_\phi$. The deformation $d_\phi$ is therefore defined as

$$d_\phi(x) = \Big(R_\phi(x) \cdot x\Big) + t_\phi(x)\,. \tag{6}$$

We employ two distinct MLP networks for our pipelines. For both architectures, we adopt a specific initialization scheme [Cai et al. 2022; Park et al. 2019] which allows the initial state of the model to predict the identity transformation without causing gradient instabilities.

*Neural field deformation.* For deforming neural fields, we follow the previous literature [Niemeyer et al. 2019; Yang et al. 2021] and define the deformed field as

$$g(x) = f_\theta\left(d_\phi^{-1}(x)\right)\,. \tag{7}$$

Intuitively, to obtain the deformed SDF value at $x$, we need to know the SDF value $f_\theta(x')$, where $x' = d_\phi(x)$. This is easily computed using the inverse of the deformation function: therefore, we employ an invertible MLP architecture based on coordinate splitting, originally proposed by Cai *et al.* [Cai et al. 2022]. Contrarily to the Lipschitz-continuous MLP used in NFGP [Yang et al. 2021], this architecture allows for an analytic expression of its inverse and thus is more efficient, as it does not require fixed point iterations for inversion. Furthermore, since this architecture is built upon the NICE model [Dinh et al. 2015], it retains its volume-preservation property, a notoriously useful prior for deformations (see Table 4). Our invertible network is composed of 6 coordinate splitting layers, where the individual coordinate processing blocks are implemented as 3-layer MLPs with Softplus activation, a hidden dimensionality of 256, and 6-frequencies Fourier features encoding [Tancik et al. 2020]. Each layer predicts a translation of the "focus" coordinate and a 2D roto-translation of the two others, which we progressively aggregate to obtain $R_\phi(x)$ and $t_\phi(x)$. The layer architecture for this model is visualized in Figure 6.

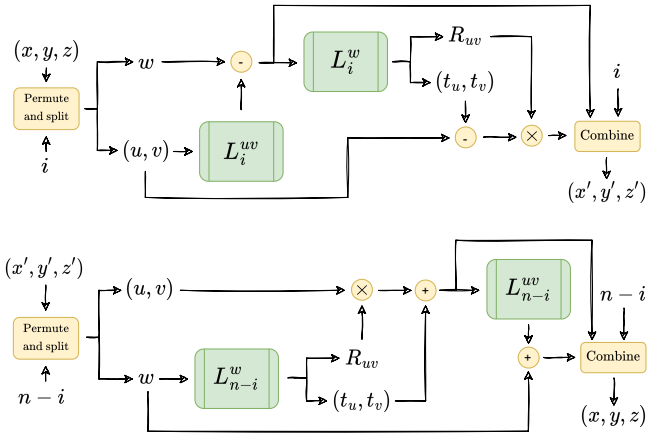



Fig. 6. Diagram for the forward (top) and inverse (bottom) passes of the invertible MLP architecture we employ in our neural field deformation pipeline. Coordinates are split and combined according to the layer index $i$ by selecting the focus coordinate $w = p_{i \bmod 3}$, where $p = (x, y, z)$ is the input vector.

*Mesh deformation.* For the mesh deformation pipeline, we do not require invertibility as we are simply interested in the forward deformation of a set of points in the zero level set of $f_\theta$. Therefore, we use a standard MLP composed of 8 linear layers with a hidden dimensionality of 256 and Softplus activation. We apply Fourier features encoding with 6 frequencies at the input layer and a residual connection at the 4th layer.

## 3.3 Optimization

Our optimization procedure is identical for both pipelines and follows previous work on neural field deformations [Yang et al. 2021]. The goal is to optimize for target handle positions while regularizing the computed deformation to have some desired properties. Given a set of handles as with source-target position pairs $H = \{(s_i, t_i)\}_{i=1}^h$ (where $s_i = t_i$ in the case of static handles), the model is constrained to fit $H$ via the simple MSE loss

$$L_{\text{handle}} = \frac{1}{h}\sum_{i=1}^{h} \left\| d_\phi(s_i) - t_i \right\|^2\,. \tag{8}$$

The key part of our loss function is the As-Rigid-As-Possible (ARAP) energy presented by Sorkine and Alexa [Sorkine and Alexa 2007].

While this formulation has already been adapted in the literature as a regularizer for generative neural models [Eisenberger et al. 2021; Huang et al. 2021], our work is the first to employ it as-is in the setting of implicit geometry processing. In practice, our goal is to ensure that our map $d$ is deforming all possible patch-based representations of the level sets of $f_\theta$ as-rigidly-as-possible. We evaluate this by sampling a set of points $\{x_k\}_{k=1}^n$, where $m \leq n$ points are sampled uniformly from the zero level set of $f_\theta$ and $n-m$ points uniformly from the bounded volume $[-1;1]^3$. A surface patch is computed using each of these points as origin, over their respective level sets, via the algorithm presented in Section 3.1, yielding a patch-based representation $\{(V_k, F)\}_{k=1}^n$. Then, our ARAP regularization is computed as

$$L_{\text{arap}} = \frac{1}{n}\sum_{k=1}^{n}\sum_{(v_i,v_j)\in E_k} w_{i,j}\left\|\left(d_\phi(v_i) - d_\phi(v_j)\right) - \left(R_\phi(v_i)\cdot(v_i - v_j)\right)\right\|^2 . \tag{9}$$

Where $E_k$ are the mesh edges for a patch mesh $(V_k, F)$ and $w_{i,j}$ are the cotangent Laplacian edge weights. Observe that we are requiring the deformed edges (left hand side of the difference) to be as close as possible to the rotation of the original edges (right hand side), effectively mitigating the action of the translation. The original ARAP formulation did not require roto-translations, as handles were fit as a pre-processing step via Laplacian smoothing of the handle function over the surface. This operation is non-trivial for implicit surfaces, and including translations ensures any handle function can be fit. In turns, this forces us to regularize the whole transformation for optimal rigidity (*i.e.*, only rotational component). The network $T_\phi$ is optimized with ADAM [Kingma and Ba 2014] steps until convergence of the loss function

$$L = \lambda_1 L_{\text{handle}} + \lambda_2 L_{\text{arap}} . \tag{10}$$

The entire procedure for computing the $L_{\text{arap}}$ loss, which we described in this section, is repeated at each iteration, including all handle points as part of the surface sample. Nonetheless, we have observed convergence to be extremely quick, typically in the order of a few hundreds of iterations, as showed in Figure 8. In our experiment, we usually trained our model for a total of 1000 steps.

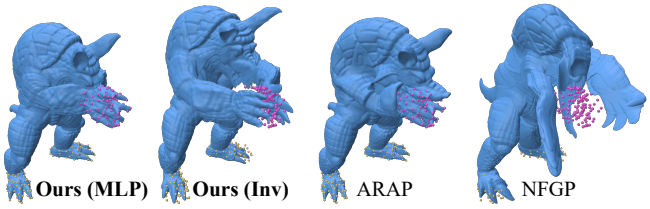



Fig. 7. Results for method and baselines for a non-invertible experiment with self-intersections, which invertible networks (Inv, NFGP) cannot represent.

## 3.4 Shape model

To represent the input shape internally to our deformation algorithm, we adopt a neural SDF model proposed in previous literature [Sitzmann et al. 2020; Tancik et al. 2020]. This model is suitable

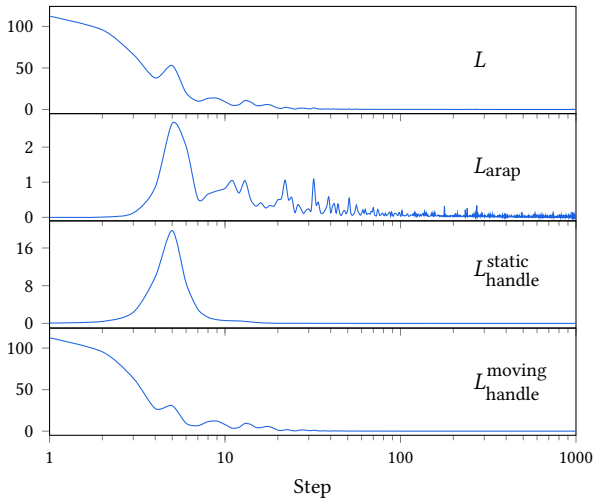



Fig. 8. Loss curves for the sculpture mesh deformation example presented in Figure 10. We show the $L_{\text{handle}}$ loss separately for the static and moving handles for visualization purposes. The trends of the curves show that convergence is achieved in a few hundred iterations.

to our application due to its efficiency on consumer-grade hardware and robustness with respect to the input geometry. The SDF is represented via a MLP network with 8 layers, a hidden dimensionality of 256, a residual connection at the fourth layer, 6-frequencies Fourier features encoding, and Softplus activation. This network is optimized via eikonal training, originally proposed by Gropp *et al.* [Gropp et al. 2020], which employs the following four losses:

$$L_{\text{zero}} = \mathbb{E}_{x\in\mathcal{S}_0}\left|f_\theta(x)\right|, \tag{11}$$

$$L_{\text{eikonal}} = \mathbb{E}_{x\in\mathbb{R}^3}\left\|\|\nabla f_\theta(x)\| - 1\right\|^2, \tag{12}$$

$$L_{\text{normals}} = \mathbb{E}_{x\in\mathcal{S}_0}\left(1 - \frac{\nabla f_\theta(x)\cdot\mathbf{n}(x)}{\|\nabla f_\theta(x)\|\|\mathbf{n}(x)\|}\right), \tag{13}$$

$$L_{\text{penalty}} = \mathbb{E}_{x\in\mathbb{R}^3}\exp\left(-\alpha\left|f_\theta(x)\right|\right) . \tag{14}$$

Defined on a discretization of the represented surface $\mathcal{S}_0$. Intuitively, these respectively constrain the network to: **a)** vanish on surface points (sampled from the input mesh triangles) **b)** have unitary norm of gradient **c)** have gradient aligned with surface normals (indicated by $\mathbf{n}(x)$ for surface point $x$), and **d)** have minimal zero level set, to avoid artefacts due to under-determination. We list the values for loss weights and $\alpha$ which we employed in our implementation in Table 2. The Adam optimizer runs for a total of 10000 steps and uses a starting learning rate of $10^{-4}$ and a scheduler which halves it at steps 1000, 2000, and 5000.

## 4 IMPLEMENTATION

We implemented our algorithm in Python, relying on PyTorch [Paszke et al. 2019] for neural network primitives, linear algebra and automatic differentiation. In addition, we used Polyscope [Sharp et al. 2019] for visualization, also extending its GUI with functionalities for easy point picking, which we used to design deformation experiments. While our viewer renders a 3D triangle mesh extracted with

marching cubes for the sake of efficiency, the points selected on the shape by the user are mapped exactly onto the implicit surface via iterations of Equation (2), allowing to select a set of continuous and accurate handles. For a given set of selected points, the user can then specify a roto-translation and save both the resulting handle transforms and the original positions. Our codebase is available at this url.

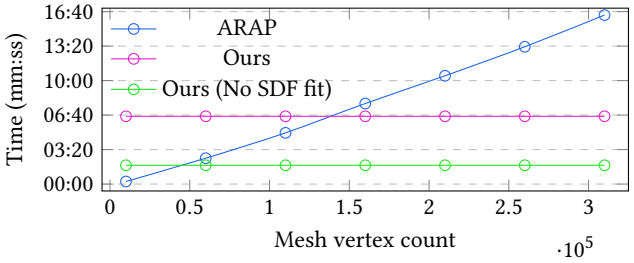



Fig. 9. Time scaling of ARAP for multiple decimations with increasing density of the sculpture mesh (Figure 10, last row) and our method, with and without SDF fitting phase.

## 5 EXPERIMENTS

*Data and baselines.* We employ two datasets in our evaluation. We constructed the first one by obtaining triangle mesh data from Thingi10k [Zhou and Jacobson 2016] and the Stanford 3D scanning repository, and designing a set of hand-crafted deformation experiments. We refer to this dataset as TFD (for Thingi-ford Deformations). The second one is the DeFAUST dataset introduced in [Maggioli et al. 2024]. The data is generated starting from the FAUST dataset [Bogo et al. 2014] by selecting shape pairs with same identity and defining handles by sparsely sampling the surface at specific locations. The original meshes are also subdivided to achieve vertex counts in the 150k-200k range. We use this data to evaluate the performance of our method against several baselines, including the CGAL [The CGAL Project 2024] implementation of three ARAP variants: the original [Sorkine and Alexa 2007] (ARAP), the spokes and rims method [Chao et al. 2010] (Elastic) and the smooth rotation variant [Levi and Gotsman 2015] (SR-ARAP). These three were used to compare performance in mesh deformation and neural field deformation (by applying them onto the discretized zero level set mesh of the input SDF field). The other baseline we employ is the neural field deformation method proposed by Yang *et al.* [Yang et al. 2021], which can similarly be applied in both facilities. For this baseline, we will indicate in the following whether the deformation is applied on the SDF field via its inverse ($\text{NFGP}_{\text{SDF}}$) or on the original input mesh ($\text{NFGP}_{\text{Mesh}}$). We also evaluate our method in various scenarios:

- $\text{Ours}^{\text{MLP}}_{\text{Mesh}}$ forward-only MLP network applied to an input mesh, after training on its SDF representation
- $\text{Ours}^{\text{Inv}}_{\text{SDF}}$ invertible network applied to an input SDF field
- $\text{Ours}^{\text{MLP}}_{\text{SDF}}$ forward-only MLP network applied to the zero level set of an input SDF field

Table 1. Hyperparameter values for the deformation procedure. $k$ and $\rho$ refer to patch density and radius, respectively, while $\lambda_i$ are the loss balancing weights.

| Data | Steps | LR | $\lambda_1$ | $\lambda_2$ | $k$ | $\rho$ |
|---|---|---|---|---|---|---|
| TFD | 1000 | $10^{-3}$ | $10^3$ | $10^1$ | 30 | $3 \cdot 10^{-2}$ |
| DeFAUST | 2000 | $10^{-3}$ | $10^3$ | $10^4$ | 30 | $10^{-2}$ |

Table 2. Hyperparameter values for the SDF fitting procedure.

| $\alpha$ | $\lambda_{\text{zero}}$ | $\lambda_{\text{eikonal}}$ | $\lambda_{\text{normals}}$ | $\lambda_{\text{penalty}}$ |
|---|---|---|---|---|
| 100 | 3000 | 100 | 50 | 3000 |

*Hardware and hyperparameters.* All of our experiments were run on a desktop computer equipped with a 12th-gen Intel Core i7-12700K (3.60GHz), 32GB of DDR4 RAM at 3600 MHz access speed, and a NVIDIA RTX4070Ti 12GB. Achieving good performance in this setting allows us to show that our method can be efficiently run even on consumer grade hardware, and therefore that it is suitable for any type of user. Where unspecified, all of our experiments were run using the hyperparameters showed in Table 1, and we used the sphere random uniform distribution to sample patch points (see Figure 3). The SDF fitting procedure is run using the hyperparameters showed in Table 2.

*Metrics.* To evaluate the **accuracy of meshing** methods with respect to some continuous implicit surface, we exploit the signed distance field $f_\theta$ and compare the respective level set value $l_i$ to $f_\theta(p)$ for surface points $p$ in the set of patches $\{\mathcal{P}_i\}_{i=1}^n$:

$$E_{\text{patch}} = \max_{i=1}^{n} \max_{p \in \mathcal{P}_i} \left| f_\theta(p) - l_i \right|. \tag{15}$$

In practice, the innermost max is approximated by evaluating the point-wise error for several points sampled from the triangles of mesh $(V_i, F)$ discretizing $\mathcal{P}_i$. The maximum is more meaningful here because a single outlier can create severe artifacts in the patch.

We use four metrics to quantitatively evaluate the computed deformations, considering both global and local aspects of the geometry. First, we consider the **percent error in volume and area** of the deformed geometry with respect to the original one. Given a surface $\mathcal{S}$ and its deformed version $\mathcal{S}'$, these are computed as

$$E_{\text{vol}} = \frac{\left| V_{\mathcal{S}} - V_{\mathcal{S}'} \right|}{V_{\mathcal{S}}}, \quad E_{\text{area}} = \frac{\left| A_{\mathcal{S}} - A_{\mathcal{S}'} \right|}{A_{\mathcal{S}}}, \tag{16}$$

where $V_{\mathcal{X}}$ and $A_{\mathcal{X}}$ indicate volume and surface area of shape $\mathcal{X}$. In order to evaluate the distortion induced on the input geometry, we use two distinct local criteria: **edge lengths and face angle errors**. To obtain consistent values across all experiments, we provide the former as a percentage of the longest edge in the source mesh. Specifically, the error is computed as

$$\text{EL} = \frac{1}{|E|} \sum_{(u,v) \in E} \frac{\left| \|u - v\| - \|d(u) - d(v)\| \right|}{\max_{e \in E} \|e\|}. \tag{17}$$

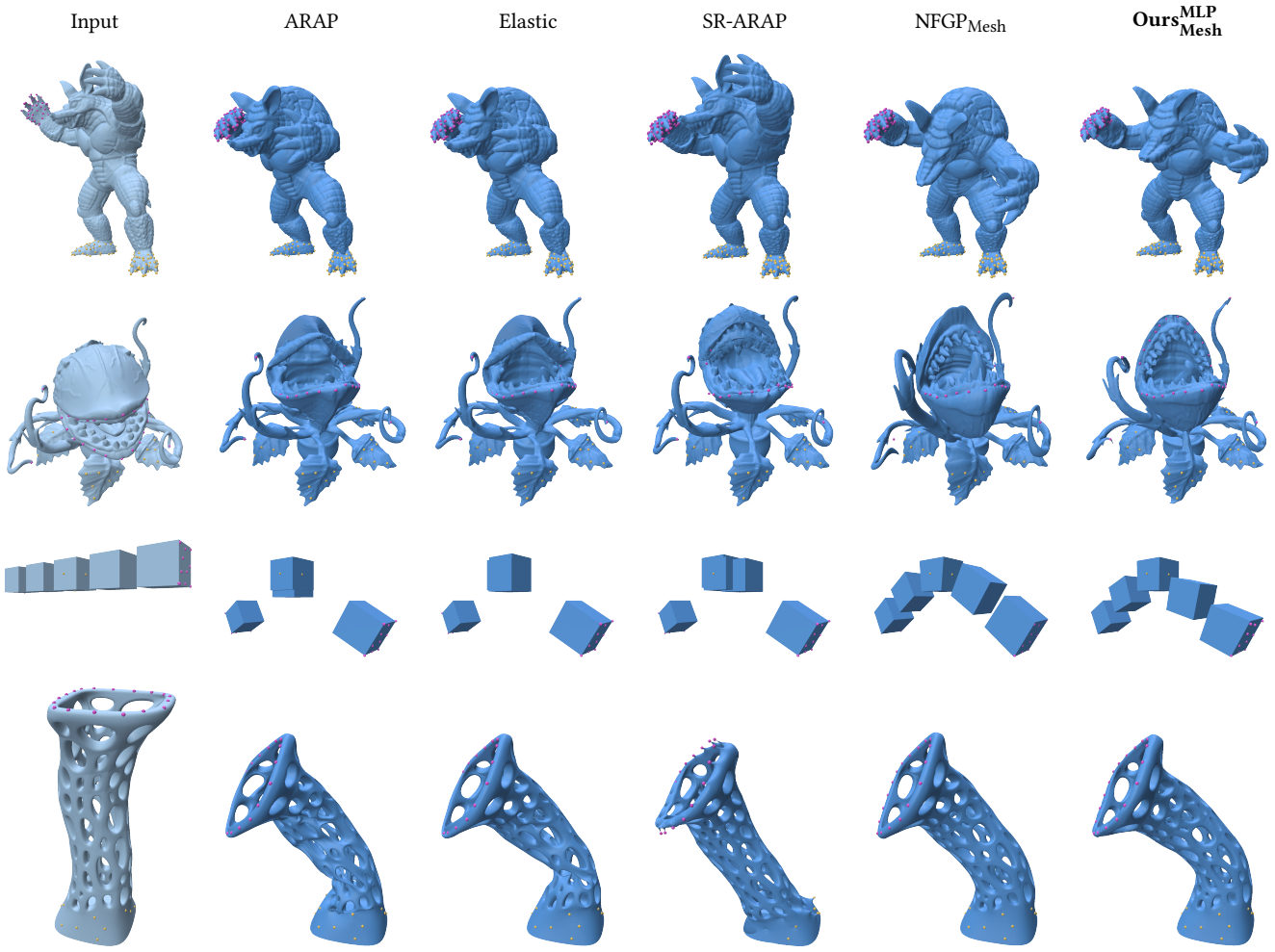



Fig. 10. Qualitative results of our method in comparison to multiple baselines for mesh deformation, on TFD examples.

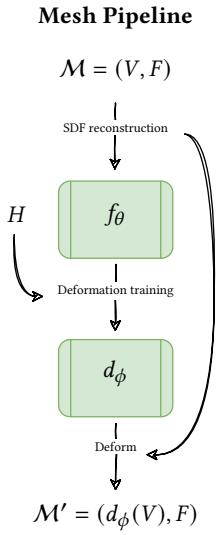
For the face angles, we compare the corresponding inner angles of source and deformed triangular faces:

$$\text{FA} = \frac{1}{3|F|} \sum_{f \in F} \sum_{(u,v) \in E(f)} \left| \cos^{-1}\left( \frac{u \cdot v}{\|u\|\|v\|} \right) - \cos^{-1}\left( \frac{d(u) \cdot d(v)}{\|d(u)\|\|d(v)\|} \right) \right| . \tag{18}$$

Both metrics require correspondence between vertex sets. To implement them for the neural field pipeline, we extract the zero level set mesh from $f_\theta$ and forward-deform its vertices.

## 5.1 High resolution mesh deformation

Our method has a very relevant application in the open problem of computing handle-guided deformations for high resolution meshes. Well-established explicit methods [Chao et al. 2010; Levi and Gotsman 2015; Sorkine and Alexa 2007] are very efficient for most realistic use-cases, but they do not scale to meshes with millions of vertices due to super-linear time and memory costs. By representing the input geometry implicitly in the weights of a neural network, and only computing Laplacian edge weights for small triangle patches, our method achieves runtime and VRAM usage independent of the input size (Figure 9) and, as highlighted in Table 3, is faster on average than explicit methods over TFD, while it is slower over DeFAUST, due to the lower average vertex count. However, the time scaling of our method is constant, as showed in Figure 9, therefore it is expected to remain efficient even at resolutions higher than those present in our evaluation.



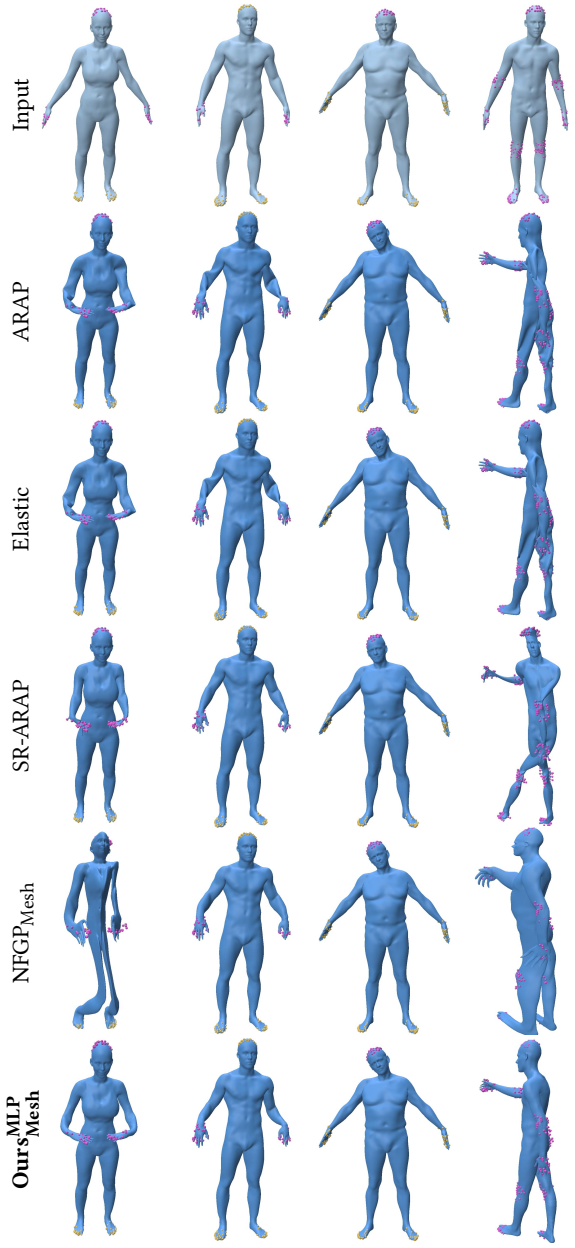



Fig. 11. Qualitative results of our method in comparison to multiple baselines for mesh deformation, on DeFAUST examples.

Moreover, most of our runtime is spent fitting the neural SDF: employing a faster procedure for this step could greatly improve our performance. The data presented in said table summarizes the performance of our method: Implicit-ARAP yields a clear improvement with respect to the baselines for most metrics. In the top block, we can observe that ARAP and its "spokes-and-rims" variant (Elastic) achieve much better metrics than our method for area, EL and FA. This is to be expected, as these methods explicitly optimize for preserving edge lengths with almost total freedom; the results for

Table 3. Average runtime, angle error (FA) and percent errors in volume, area, and edge lengths (EL) for our high-resolution mesh deformation experiments. The time for our method and NFGP includes 4m:44s required for the initial neural SDF fit, meaning our deformation phase runs takes 1m:49s on average for 1000 steps. TFD results are averaged over all examples supported by the CGAL implementation of ARAP baselines, to which we removed the octopus example (see Figure 12) due to out-of-scale metric values.

| | | Volume | Area | EL | FA | Time |
|---|---|---|---|---|---|---|
| TFD | **Ours** | 4.27% | 2.83% | 0.76% | 3.448° | 6m:33s |
| | NFGP | 8.41% | 7.04% | 0.87% | 4.178° | 14h:31m |
| | ARAP | 11.82% | 0.23% | 0.12% | 0.486° | 8m:06s |
| | Elastic | 11.42% | 0.25% | 0.12% | 0.495° | 8m:00s |
| | SR-ARAP | 8.24% | 3.46% | 0.89% | 4.743° | 9m:07s |
| DeFAUST | **Ours** | 0.99% | 0.82% | 1.06% | 1.517° | 8m:22s |
| | NFGP | 15.02% | 20.25% | 8.71% | 8.859° | 14h:31m |
| | ARAP | 12.41% | 0.45% | 0.37% | 0.517° | 7m:15s |
| | Elastic | 12.25% | 0.45% | 0.38% | 0.523° | 8m:27s |
| | SR-ARAP | 11.69% | 5.36% | 3.39% | 5.628° | 7m:11s |

SR-ARAP show that simply including a smoothness prior on the computed rotations aligns the scale of the error values to ours. Combining these quantities with the qualitative evaluation we present in Figures 10 and 11 provides a clear picture of the accuracy, robustness and efficiency of our method, which consistently yields accurate results with minimal artefacts. We point out that the results of ARAP baselines for the cubes experiment are correct, in the sense that the unconstrained 2nd and 4th cubes can be mapped arbitrarily. Implicit-ARAP and NFGP, on the other hand, exploit the spectral bias of neural networks to propagate the handle maps smoothly over the whole volume. However, NFGP deforms the individual cubes into trapezoids more evidently than our method. The last advantage in using an implicit method like ours lies in its independence on the quality of the input shape's connectivity: the CGAL implementation of the explicit baselines failed to run experiments using the original buddha mesh (see Figure 17), which was also the most dense one in our experiments counting ~550k vertices. Lastly, Figure 7 motivates the usage of a non-invertible MLP network for this pipeline: the visualizations show that using invertible architectures does not allow to define non-bijective transformations of the input shape, which may instead be easily obtained by the original ARAP method or our mesh deformation pipeline using the MLP network.

## 5.2 Neural field deformation

Another application of Implicit-ARAP is in implicit geometry processing, specifically handle-guided deformation of neural implicit surfaces. The problem was first introduced by Yang *et al.* [Yang et al. 2021], but the literature is missing follow-up proposals of significant improvements over their work. Berzins *et al.* [Berzins et al. 2023] hint at neural shape editing as one of the applications of their method, but a complete implementation is not available. Other baselines are obtained by applying explicit methods on the zero level set of a neural field, albeit these methods do not preserve the neural field information. We show averaged quantitative results for our method and baselines in Table 4. For true implicit methods (Ours and NFGP), we compute volume and area directly

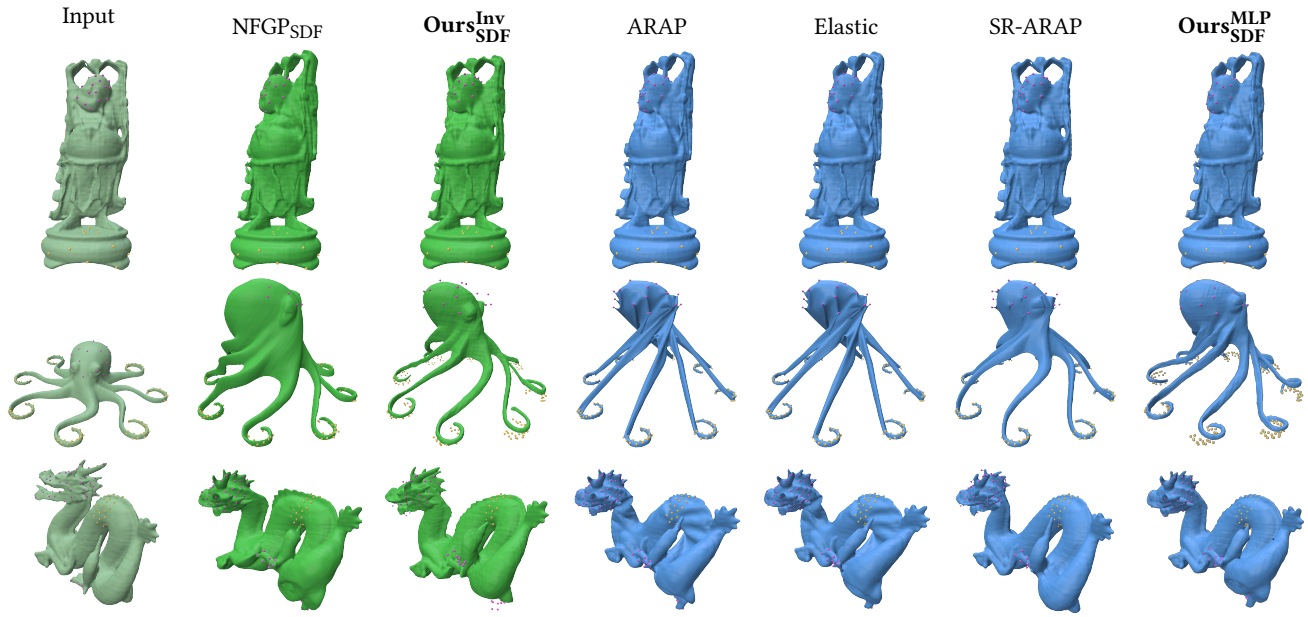



Fig. 12. Qualitative results of our method in comparison to multiple baselines for neural field deformation. Discrete methods [Chao et al. 2010; Levi and Gotsman 2015; Sorkine and Alexa 2007] are applied by extracting the marching cubes mesh at resolution $R = 512$ and applying a remeshing step, as suggested in [Yang et al. 2021] due to marching cube triangulations not matching ARAP assumptions. We show proper implicit deformations in green (*i.e.*, the zero level set of the deformed field is visualized) while deformations applied on the zero-level set mesh (extracted with marching cubes) are rendered in blue. Inv/MLP superscripts indicate whether the invertible or MLP networks (respectively) are employed in the examples.

from the deformed field $g$. For the EL and FA metrics we deform the zero level set mesh of $f_\theta$, because they require consistent connectivity; the same holds for the discrete methods ARAP, Elastic and SR-ARAP. The meshes for these methods were extracted with marching cubes resolution $R = 512$. From the data presented in the table, we observe that our method achieves optimal volume error due to the employed architecture being volume-preserving. Furthermore, the performance in preservation of topology properties such as edge lengths and face angles degraded for both NFGP and our method. We believe this could be due to the marching cubes triangulations which were previously shown to hinder vanilla ARAP results [Yang et al. 2021]. This can be easily noticed in Figure 12. Combining the results in Table 4 with the visualizations, we can appreciate how our method reliably yields plausible results in a fraction of the time required by the baselines, especially NFGP. We note that this pipeline accepts a neural SDF as input, thus the time for SDF fitting is not to be considered.

**Neural Field Pipeline**

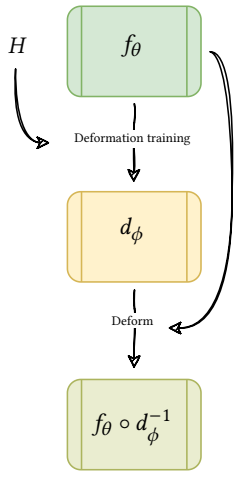



Table 4. Average runtime, angle error (FA) and percent errors in volume, area, and edge lengths (EL) for our neural field deformation experiments. Explicit ARAP baselines are run using the zero level set marching cubes mesh as input. TFD results do not include the octopus experiment (see Figure 12) due to out-of-scale metric values.

| | | Volume | Area | EL | FA | Time |
|---|---|---|---|---|---|---|
| TFD | **Ours** | 0.00% | 0.85% | 3.26% | 4.541° | 2m:48s |
| | NFGP | 6.66% | 5.30% | 3.34% | 3.516° | 14h:26m |
| | ARAP | 9.40% | 0.29% | 0.33% | 0.358° | 9m:51s |
| | Elastic | 9.01% | 0.30% | 0.38% | 0.379° | 9m:44s |
| | SR-ARAP | 5.60% | 3.97% | 3.44% | 4.615° | 10m:27s |
| DeFAUST | **Ours** | 0.00% | 0.63% | 2.41% | 3.399° | 5m:36s |
| | NFGP | 15.15% | 20.02% | 9.63% | 7.577° | 14h:26m |
| | ARAP | 17.36% | 16.44% | 5.72% | 1.677° | 8m:11s |
| | Elastic | 17.33% | 16.41% | 5.73% | 1.683° | 8m:38s |
| | SR-ARAP | 12.09% | 8.67% | 8.45% | 6.833° | 7m:06s |

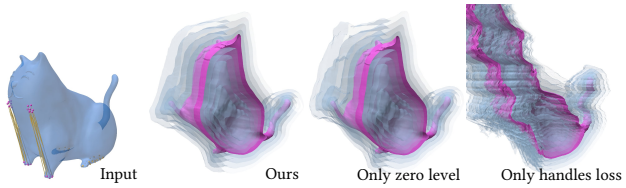



Fig. 13. Qualitative ablation study for our method. Left to right: input, neural field deformation pipeline result, results with zero level set patches only, results with handles loss only.

The difference in time with the mesh deformation pipeline is due to the architecture: the invertible network is 54% more computationally expensive to query. Lastly, Figure 13 shows the benefits of both computing local patches for all level sets and employing the ARAP regularization for our deformation network.

### 5.3 Local patch meshing

Lastly, we devote a section of our experiments to evaluating our local patch meshing algorithm. We begin by highlighting that **our method should not be considered as a drop-in replacement for marching cubes**: even by sampling a very large number of patches, it is unlikely to cover the entire surface, and a set of largely overlapping patches is not in general a useful representation for the surface. Instead, our method generates discretizations of local surface regions, and we are interested to a) verify how accurately these patches represent the underlying geometry and b) provide indications on how to select useful radius and density values for deformation tasks.

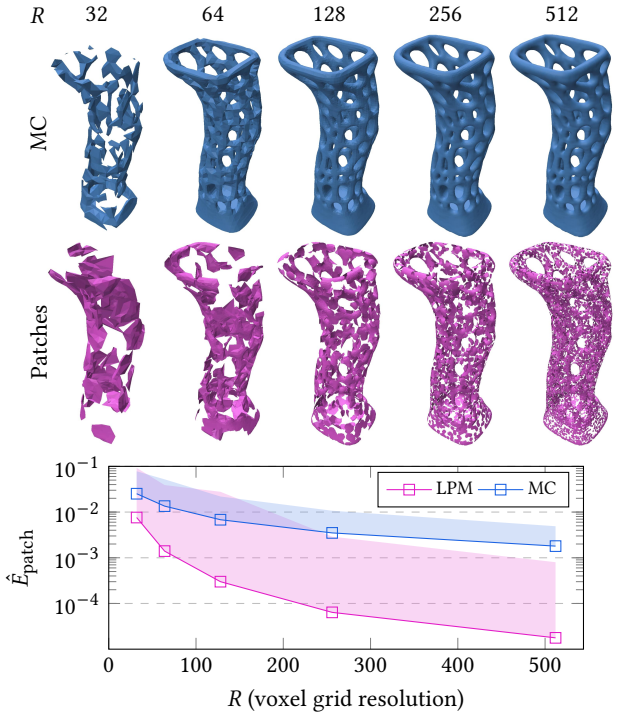



Fig. 14. Qualitative results and numerical evaluation of the accuracy of our local patching method against the Marching Cubes algorithm. We construct the local patch meshes in this experiment to have similar vertex count and identical average edge length to the corresponding marching cubes triangulation. The per-patch vertex count is fixed at 30 for all resolutions.

*Reconstruction Ability.* In Figure 14 we compare marching cubes meshes to local patch meshes constructed to approximate their vertex count and average edge length. The renders show the change in "coarseness" of our representation with respect to the resolution

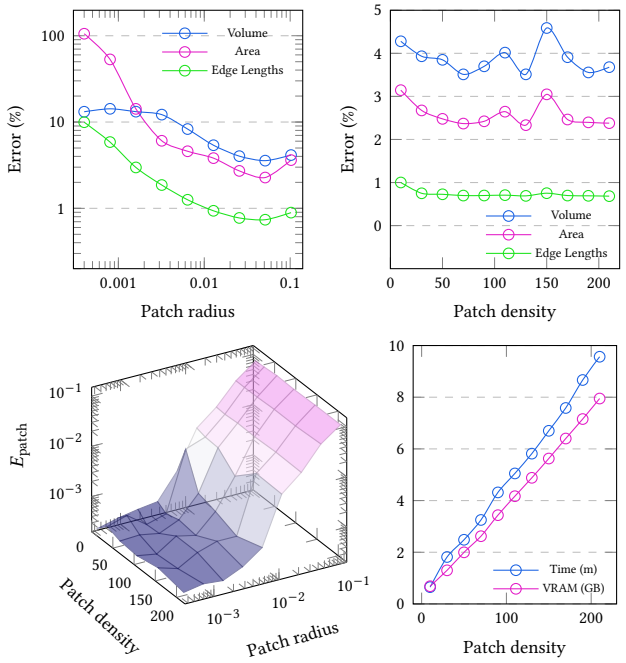



Fig. 15. Patch scaling experiments, averaged over our TFD dataset. **Top left**: change in deformation error metrics, varying patch radius. Patch density is fixed at 30. **Top right**: change in deformation error metrics, varying patch density. Patch radius is fixed at 0.03. **Bottom left**: Change in SDF reconstruction error (Equation (15)) with respect to patch vertex count and patch radius. **Bottom right**: time and GPU memory scaling for our deformation algorithm, varying patch density.

and the graph below provides some insights to the accuracy of local patch meshing. The line plot shows the *average* approximation error

$$\hat{E}_{\text{patch}} = \frac{1}{n}\sum_{i=1}^{n} \mathbb{E}_{p\in\mathcal{P}_i}\left|f_\theta(p) - l_i\right|, \tag{19}$$

while the shaded areas cover the entire regions between $\hat{E}_{\text{patch}}$ and the maximum error $E_{\text{patch}}$ as defined in Equation (15). For marching cubes, these metrics can be computed by considering the entire mesh as a patch (*i.e.*, $n = 1$ and $\mathcal{P}_1$ is the marching cubes mesh). Despite the marching cubes line hinting at a lower deviation from the mean, our method achieves much lower average error even for very wide patches. This is because the patch vertices are mapped exactly onto the surface, while marching cubes places triangles based on how the surface crosses the sampled voxels; therefore, our error only depends on the overall size of the patch relative to how flat the approximated local surface region is.

*Approximation Error and Deformation Quality.* The bottom left plot in Figure 15 shows how patch radius and density impact the approximation error. We observe a very consistent behaviour when changing the patch density, where values above 50 does not reflect in significant improvements in accuracy. The variation in error metrics (see top right plot) for increasing patch density is not sufficient to justify the additional cost in time and memory (see bottom right

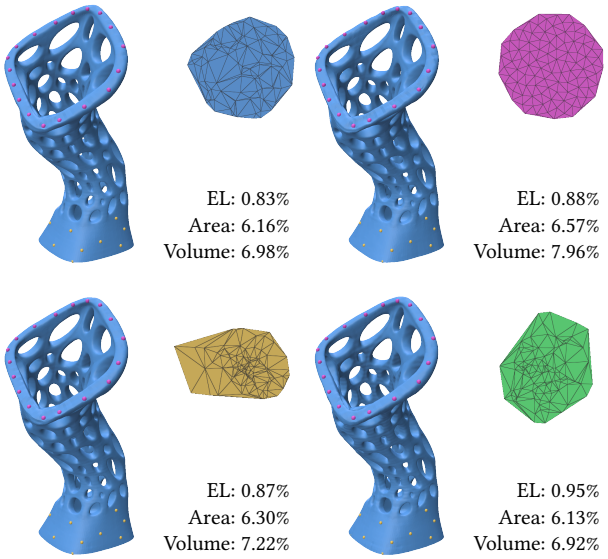



Fig. 16. Mesh deformation results for multiple patch distributions. The final results are qualitatively identical and the variations in metrics are negligible in most cases. The input shape is showed in the last row of Figure 10.

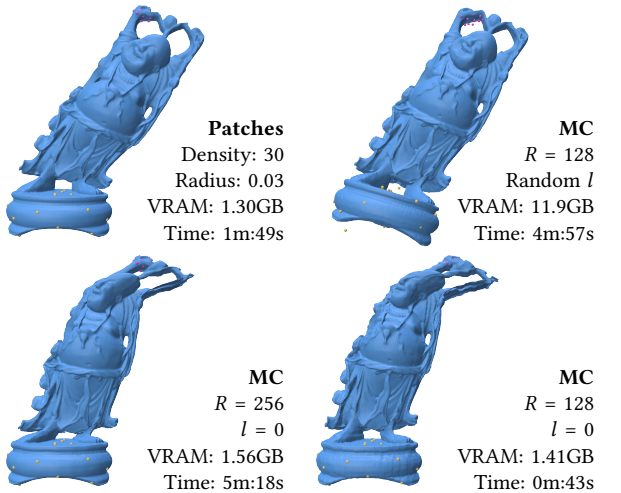



Fig. 17. LPM and MC as underlying triangulation for deformation tasks. Our sampling is both memory efficient and expressive.

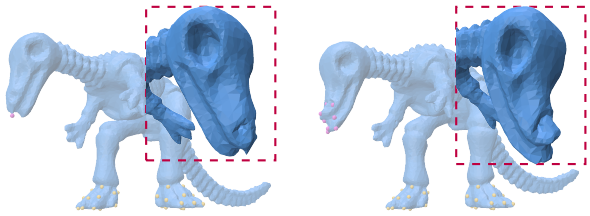


Fig. 18. Results of our method for the dino experiment, with 1 (left) and 10 (right) handles on the snout. While having a single handle may results in the "spike" artifact you can observe in the left closeup, increasing the number of handles has a smoothing effect. However, the model could have to sacrifice some measure of local rigidity to fit a constant translation on multiple handles (see right closeup).

plot), therefore a conservative choice appears to be the best one. In our experiments, radius values around 0.01 would usually provide geometrically meaningful patches without significant artefacts – we do not use relative units for the radius since all shapes are normalized in the unit cube. On the other hand, while smaller radius values reduce the approximation error, the patches tend to collapse to single points as their radius approaches zero. This results in a less expressive representation of the local geometry, which negatively affects the deformation results as showed in the top left plot of Figure 15. Lastly, overly large patches also cause a degradation in performance due to the increase in approximation error.

*Discretization.* In Figure 17, we present qualitative results of mesh deformation using both patches and marching cubes (MC) as underlying discretizations for ARAP energy. We show three different variations for MC: zero level set only with resolution $R = 256$, zero level set only with resolution $R = 128$, and meshing all level sets with $R = 128$ to make the computed energy similar to that of our method. The last option leads to meshes with very high triangle count especially for higher SDF values which increases the memory requirement and can only be done for $R = 128$, which seems to be too coarse for the optimization and does not fulfill all constraints. Using only zero level set, it fails to produce a smooth deformation due to lack of regularization over the whole domain. Overall, our patching approach appears more stable, reliable, and efficient. Moreover, the results presented in Figure 16 suggest that the variation in error metrics due to the choice in patch point sampling is negligible.

## 6 CONCLUSIONS

We presented a novel way to apply as-rigid-as-possible deformations to neural fields which is highly efficient and more flexible and robust than previous work. To this end, we proposed to mesh patches from several isosurfaces of a signed distance field and then compute the energy on those to regularize a deformation field encoded in a neural network. This has important advantages because it detaches the computational complexity from the resolution and allows for regularization that includes properties of the embedding space, *e.g.*, the volume-preservation of our invertible model. The core idea can be applied seamlessly in the context of deforming high resolution meshes and neural fields: in the latter case, we employ an invertible deformation which allows to define the output neural field, at the cost of generality. The combination of these properties - directly inferring the new SDF and general deformation space - is hard to obtain due to the unpredictable possible changes in the SDF from an unconstrained deformation, but it would make for a challenging future work. In the context of mesh deformation, we believe that

employing more efficient neural SDF representations provides an interesting direction for future investigation. Nevertheless, we believe our work is a valuable step in the direction of efficient and flexible editing of neural fields, and that our local discretization could be applied to solve more geometric problems in the implicit domain.

## REFERENCES


Arturs Berzins, Moritz Ibing, and Leif Kobbelt. 2023. Neural Implicit Shape Editing using Boundary Sensitivity. arXiv:2304.12951 [cs.CV]

Federica Bogo, Javier Romero, Matthew Loper, and Michael J. Black. 2014. FAUST: Dataset and Evaluation for 3D Mesh Registration. In *2014 IEEE Conference on Computer Vision and Pattern Recognition*. 3794–3801. https://doi.org/10.1109/CVPR.2014.491

Mario Botsch, Robert W. Sumner, Mark Pauly, and Markus Gross. 2006. Deformation Transfer for Detail-Preserving Surface Editing. In *Vision, modeling, and visualization 2006 : proceedings, November 22-24, 2006, Aachen, Germany*. Akademische Verlagsgesellschaft, Berlin, 357 – 364.

Aljaz Bozic, Pablo Palafox, Michael Zollhöfer, Angela Dai, Justus Thies, and Matthias Nießner. 2020. Neural non-rigid tracking. *Advances in Neural Information Processing Systems* 33 (2020), 18727–18737.

Hongrui Cai, Wanquan Feng, Xuetao Feng, Yan Wang, and Juyong Zhang. 2022. Neural Surface Reconstruction of Dynamic Scenes with Monocular RGB-D Camera. In *Thirty-sixth Conference on Neural Information Processing Systems (NeurIPS)*.

Isaac Chao, Ulrich Pinkall, Patrick Sanan, and Peter Schröder. 2010. A simple geometric model for elastic deformations. *ACM Trans. Graph.* 29, 4, Article 38 (jul 2010), 6 pages. https://doi.org/10.1145/1778765.1778775

Yiwen Chen, Zilong Chen, Chi Zhang, Feng Wang, Xiaofeng Yang, Yikai Wang, Zhongang Cai, Lei Yang, Huaping Liu, and Guosheng Lin. 2023. GaussianEditor: Swift and Controllable 3D Editing with Gaussian Splatting. arXiv:2311.14521 [cs.CV]

Julian Chibane, Aymen Mir, and Gerard Pons-Moll. 2020. Neural Unsigned Distance Fields for Implicit Function Learning. In *Advances in Neural Information Processing Systems (NeurIPS)*.

Laurent Dinh, David Krueger, and Yoshua Bengio. 2015. NICE: Non-linear Independent Components Estimation. In *3rd International Conference on Learning Representations, ICLR 2015, San Diego, CA, USA, May 7-9, 2015, Workshop Track Proceedings*, Yoshua Bengio and Yann LeCun (Eds.). http://arxiv.org/abs/1410.8516

Marvin Eisenberger, Zorah Lähner, and Daniel Cremers. 2019. Divergence-Free Shape Correspondence by Deformation. *Computer Graphics Forum* 38, 5 (2019), 1–12. https://doi.org/10.1111/cgf.13785 arXiv:https://onlinelibrary.wiley.com/doi/pdf/10.1111/cgf.13785

Marvin Eisenberger, David Novotny, Gael Kerchenbaum, Patrick Labatut, Natalia Neverova, Daniel Cremers, and Andrea Vedaldi. 2021. NeuroMorph: Unsupervised Shape Interpolation and Correspondence in One Go. In *Proceedings of the IEEE/CVF Conference on Computer Vision and Pattern Recognition*. 7473–7483.

Ziya Erkoç, Fangchang Ma, Qi Shan, Matthias Nießner, and Angela Dai. 2023. HyperDiffusion: Generating Implicit Neural Fields with Weight-Space Diffusion. In *International Conference on Computer Vision (ICCV)*.

Janick Martinez Esturo, Christian Rössl, and Holger Theisel. 2010. Continuous Deformations of Implicit Surfaces. In *Vision, Modeling, and Visualization (2010)*, Reinhard Koch, Andreas Kolb, and Christof Rezk-Salama (Eds.). The Eurographics Association. https://doi.org/10.2312/PE/VMV/VMV10/219-226

Jiemin Fang, Junjie Wang, Xiaopeng Zhang, Lingxi Xie, and Qi Tian. 2024. GaussianEditor: Editing 3D Gaussians Delicately with Text Instructions. In *CVPR*.

Amos Gropp, Lior Yariv, Niv Haim, Matan Atzmon, and Yaron Lipman. 2020. Implicit Geometric Regularization for Learning Shapes. In *Proceedings of Machine Learning and Systems 2020*. 3569–3579.

Qixing Huang, Xiangru Huang, Bo Sun, Zaiwei Zhang, Junfeng Jiang, and Chandrajit Bajaj. 2021. ARAPReg: An As-Rigid-As Possible Regularization Loss for Learning Deformable Shape Generators. In *2021 IEEE/CVF International Conference on Computer Vision (ICCV)*. IEEE Computer Society, Los Alamitos, CA, USA, 5795–5805. https://doi.org/10.1109/ICCV48922.2021.00576

Diederik P. Kingma and Jimmy Ba. 2014. Adam: A Method for Stochastic Optimization. *CoRR* abs/1412.6980 (2014). https://api.semanticscholar.org/CorpusID:6628106

Zohar Levi and Craig Gotsman. 2015. Smooth Rotation Enhanced As-Rigid-As-Possible Mesh Animation. *IEEE Transactions on Visualization and Computer Graphics* 21, 2 (2015), 264–277. https://doi.org/10.1109/TVCG.2014.2359463

Minghua Liu, Minhyuk Sung, Radomir Mech, and Hao Su. 2021a. DeepMetaHandles: Learning Deformation Meta-Handles of 3D Meshes With Biharmonic Coordinates. In *Proceedings of the IEEE/CVF Conference on Computer Vision and Pattern Recognition (CVPR)*. 12–21.

Steven Liu, Xiuming Zhang, Zhoutong Zhang, Richard Zhang, Jun-Yan Zhu, and Bryan Russell. 2021b. Editing Conditional Radiance Fields. In *Proceedings of the International Conference on Computer Vision (ICCV)*.

W. Liu, Y. Wu, S. Ruan, and G. S. Chirikjian. 2023. Marching-Primitives: Shape Abstraction from Signed Distance Function. In *2023 IEEE/CVF Conference on Computer Vision and Pattern Recognition (CVPR)*. IEEE Computer Society, Los Alamitos, CA, USA, 8771–8780. https://doi.org/10.1109/CVPR52729.2023.00847

William E. Lorensen and Harvey E. Cline. 1987a. Marching cubes: A high resolution 3D surface construction algorithm. *SIGGRAPH Comput. Graph.* 21, 4 (aug 1987), 163–169. https://doi.org/10.1145/37402.37422

William E. Lorensen and Harvey E. Cline. 1987b. Marching cubes: A high resolution 3D surface construction algorithm. In *Proceedings of the 14th Annual Conference on Computer Graphics and Interactive Techniques (SIGGRAPH '87)*. Association for Computing Machinery, New York, NY, USA, 163–169. https://doi.org/10.1145/37401.37422

Filippo Maggioli, Daniele Baieri, Zorah Lähner, and Simone Melzi. 2024. SShaDe: a framework for scalable shape deformation via local representations. arXiv:2409.17961 [cs.GR] https://arxiv.org/abs/2409.17961

Ishit Mehta, Manmohan Chandraker, and Ravi Ramamoorthi. 2022. A Level Set Theory for Neural Implicit Evolution under Explicit Flows. In *European Conference on Computer Vision (ECCV)*.

Ben Mildenhall, Pratul P. Srinivasan, Matthew Tancik, Jonathan T. Barron, Ravi Ramamoorthi, and Ren Ng. 2020. NeRF: Representing Scenes as Neural Radiance Fields for View Synthesis. In *ECCV*.

Yuichi Nagata and Shinji Imahori. 2024. Creation of Dihedral Escher-like Tilings Based on As-Rigid-As-Possible Deformation. *ACM Transactions on Graphics* 43, 2 (2024), 1–18.

Michael Niemeyer, Lars Mescheder, Michael Oechsle, and Andreas Geiger. 2019. Occupancy Flow: 4D Reconstruction by Learning Particle Dynamics. In *Proc. of the IEEE International Conf. on Computer Vision (ICCV)*.

Tiago Novello, Vinícius da Silva, Guilherme Schardong, Luiz Schirmer, Hélio Lopes, and Luiz Velho. 2023. Neural Implicit Surface Evolution. In *Proceedings of the IEEE/CVF International Conference on Computer Vision (ICCV)*. 14279–14289. https://openaccess.thecvf.com/content/ICCV2023/html/Novello_Neural_Implicit_Surface_Evolution_ICCV_2023_paper.html

Francesco Palandra, Andrea Sanchietti, Daniele Baieri, and Emanuele Rodolà. 2024. GSEdit: Efficient Text-Guided Editing of 3D Objects via Gaussian Splatting. arXiv:2403.05154 [cs.CV] https://arxiv.org/abs/2403.05154

Xiaoyu Pan, Jiaming Mai, Xinwei Jiang, Dongxue Tang, Jingxiang Li, Tianjia Shao, Kun Zhou, Xiaogang Jin, and Dinesh Manocha. 2022. Predicting Loose-Fitting Garment Deformations Using Bone-Driven Motion Networks. In *ACM SIGGRAPH 2022 Conference Proceedings*.

Nikolas Paries, Patrick Degener, and Reinhard Klein. 2007. Simple and Efficient Mesh Editing with Consistent Local Frames. In *15th Pacific Conference on Computer Graphics and Applications (PG'07)*. 461–464. https://doi.org/10.1109/PG.2007.43

Jeong Joon Park, Peter Florence, Julian Straub, Richard Newcombe, and Steven Lovegrove. 2019. DeepSDF: Learning Continuous Signed Distance Functions for Shape Representation. In *The IEEE Conference on Computer Vision and Pattern Recognition (CVPR)*.

Adam Paszke, Sam Gross, Francisco Massa, Adam Lerer, James Bradbury, Gregory Chanan, Trevor Killeen, Zeming Lin, Natalia Gimelshein, Luca Antiga, Alban Desmaison, Andreas Köpf, Edward Yang, Zach DeVito, Martin Raison, Alykhan Tejani, Sasank Chilamkurthy, Benoit Steiner, Lu Fang, Junjie Bai, and Soumith Chintala. 2019. *PyTorch: an imperative style, high-performance deep learning library*. Curran Associates Inc., Red Hook, NY, USA.

Albert Pumarola, Enric Corona, Gerard Pons-Moll, and Francesc Moreno-Noguer. 2020. D-NeRF: Neural Radiance Fields for Dynamic Scenes. In *Proceedings of the IEEE/CVF Conference on Computer Vision and Pattern Recognition*.

Nicholas Sharp et al. 2019. Polyscope. www.polyscope.run.

Vincent Sitzmann, Julien N.P. Martel, Alexander W. Bergman, David B. Lindell, and Gordon Wetzstein. 2020. Implicit Neural Representations with Periodic Activation Functions. In *Proc. NeurIPS*.

Olga Sorkine and Marc Alexa. 2007. As-Rigid-As-Possible Surface Modeling. In *Proceedings of EUROGRAPHICS/ACM SIGGRAPH Symposium on Geometry Processing*. 109–116.

Matthew Tancik, Pratul P. Srinivasan, Ben Mildenhall, Sara Fridovich-Keil, Nithin Raghavan, Utkarsh Singhal, Ravi Ramamoorthi, Jonathan T. Barron, and Ren Ng. 2020. Fourier Features Let Networks Learn High Frequency Functions in Low Dimensional Domains. *NeurIPS* (2020).

The CGAL Project. 2024. *CGAL User and Reference Manual* (5.6.1 ed.). CGAL Editorial Board. https://doc.cgal.org/5.6.1/Manual/packages.html

Holger Theisel. 2002. Exact Isosurfaces for Marching Cubes. *Computer Graphics Forum* 21, 1 (2002), 19–32. https://doi.org/10.1111/1467-8659.00563 arXiv:https://onlinelibrary.wiley.com/doi/pdf/10.1111/1467-8659.00563

Amir Vaxman, Christian Müller, and Ofir Weber. 2015. Conformal mesh deformations with Möbius transformations. *ACM Transactions on Graphics (TOG)* 34 (2015), 1 – 11.

Can Wang, Menglei Chai, Mingming He, Dongdong Chen, and Jing Liao. 2021. CLIP-NeRF: Text-and-Image Driven Manipulation of Neural Radiance Fields. *2022*

*IEEE/CVF Conference on Computer Vision and Pattern Recognition (CVPR)* (2021), 3825–3834. https://api.semanticscholar.org/CorpusID:245006265

Guandao Yang, Serge Belongie, Bharath Hariharan, and Vladlen Koltun. 2021. Geometry Processing with Neural Fields. In *Advances in Neural Information Processing Systems*, M. Ranzato, A. Beygelzimer, Y. Dauphin, P.S. Liang, and J. Wortman Vaughan (Eds.), Vol. 34. Curran Associates, Inc., 22483–22497. https://proceedings.neurips.cc/paper_files/paper/2021/file/bd686fd640be98efaae0091fa301e613-Paper.pdf

Yizhou Yu, Kun Zhou, Dong Xu, Xiaohan Shi, Hujun Bao, Baining Guo, and Heung-Yeung Shum. 2004. Mesh editing with poisson-based gradient field manipulation. *ACM Trans. Graph.* 23, 3 (aug 2004), 644–651.

Qingnan Zhou and Alec Jacobson. 2016. Thingi10K: A Dataset of 10, 000 3D-Printing Models. *CoRR* abs/1605.04797 (2016). arXiv:1605.04797 http://arxiv.org/abs/1605.04797